Three#Tier Hierarchical Structures for Extreme Pool Boiling Heat Transfer Performance

Citation: Song, Youngsup, Díaz#Marín, Carlos D, Zhang, Lenan, Cha, Hyeongyun, Zhao, Yajing et al. 2022. "Three#Tier Hierarchical Structures for Extreme Pool Boiling Heat Transfer Performance." Advanced Materials, 34 (32).

As Published: 10.1002/adma.202200899

Publisher: Wiley

Persistent URL: https://hdl.handle.net/1721.1/145704

Version: Final published version: final published article, as it appeared in a journal, conference proceedings, or other formally published context

RESEARCH ARTICLE

ADVANCED MATERIALS
www.advmat.de

Three-Tier Hierarchical Structures for Extreme Pool Boiling Heat Transfer Performance

*Youngsup Song, Carlos D. Díaz-Marín, Lenan Zhang, Hyeongyun Cha, Yajing Zhao, and Evelyn N. Wang**

Boiling is an effective energy-transfer process with substantial utility in energy applications. Boiling performance is described mainly by the heat-transfer coefficient (HTC) and critical heat flux (CHF). Recent efforts for the simultaneous enhancement of HTC and CHF have been limited by an intrinsic trade-off between them—HTC enhancement requires high nucleation-site density, which can increase bubble coalescence resulting in limited CHF enhancement. In this work, this trade-off is overcome by designing three-tier hierarchical structures. The bubble coalescence is minimized to enhance the CHF by defining nucleation sites with microcavities interspersed within hemi-wicking structures. Meanwhile, the reduced nucleation-site density is compensated for by incorporating nanostructures that promote evaporation for HTC enhancement. The hierarchical structures demonstrate the simultaneous enhancement of HTC and CHF up to 389% and 138%, respectively, compared to a smooth surface. This extreme boiling performance can lead to significant energy savings in a variety of boiling applications.

1. Introduction

The global demand for electrical power has been continuously growing ≈3% annually during the past decade.[1] Over 90% of this electrical power is generated by steam turbines,[2] where boiling generates the steam. Steam generation is also essential in sustainability such as for food and chemical processing, water purification, sterilization, and harvesting.[3] Furthermore, the high heat dissipation capability of boiling enables such processes for thermal management of high flux energy applications such as concentrated photovoltaics, fast-charging batteries, data centers, and integrated electronics.[4] The continuing growth in energy demands puts an increased emphasis on achieving even larger enhancements in boiling performance.

The heat transfer coefficient (HTC, h) and critical heat flux (CHF, q''_{CHF}) are two major parameters that quantify boiling performance. The HTC describes the efficiency of boiling heat transfer, defined as the ratio of heat flux (q'') to the wall superheat (ΔT_{w}), that is, $h = q''/\Delta T_{\mathrm{w}}$. Here ΔT_{w} is the temperature difference between the boiling surface and the saturated liquid. In the nucleate boiling regime, the heat flux increases with the wall superheat. However, when the heat flux is sufficiently high, excessive vapor bubbles nucleated on the boiling surface prevent the liquid from rewetting the surface and, in turn, form an insulating vapor film over the surface. This vapor film becomes a thermal barrier that leads to a drastic increase in wall superheat and burnout of a boiling system. This transition from nucleate boiling to film boiling is known as the boiling crisis, where the maximum heat flux is CHF. Enhancing CHF, therefore, can either enable larger safety margins or extend the operational heat flux range for boiling systems.[5]

Recent efforts to enhance boiling heat transfer have focused on engineering the working fluid or surface properties.[6] In particular, engineering surface structures have received greater attention owing to the constraints on chemical compatibility or operational conditions which can limit the choice of the working fluid. Representative examples of surface structures that effectively enhance CHF are known to be hemi-wicking surfaces such as micropillars and nanowires.[7] These structures enhance CHF by harnessing thin-film evaporation around pillars and capillary-fed wicking through the structures.[8] Surfaces with microcavities, on the other hand, have shown improved HTC by trapping vapor embryos that promote nucleation.[9] Recently, a combination of microtube and micropillar structures referred to as tube-clusters in pillars (TIP), has shown the ability to tune the HTC and CHF by controlling bubble coalescence while maintaining capillary wicking.[10] Despite the controllability, achieving extreme enhancement of HTC and CHF simultaneously remains challenging due to the intrinsic trade-off between HTC and CHF associated with nucleation-site density. For example, high nucleation-site density may increase HTC but decrease CHF because extensive bubble coalescence hinders the capillary wicking performance, while the reduced number of nucleation sites will limit the HTC enhancement.

Y. Song, C. D. Díaz-Marín, L. Zhang, H. Cha, Y. Zhao, E. N. Wang
Department of Mechanical Engineering
Massachusetts Institute of Technology
Cambridge, MA 02139, USA
E-mail: enwang@mit.edu

The ORCID identification number(s) for the author(s) of this article can be found under https://doi.org/10.1002/adma.202200899.

DOI: 10.1002/adma.202200899

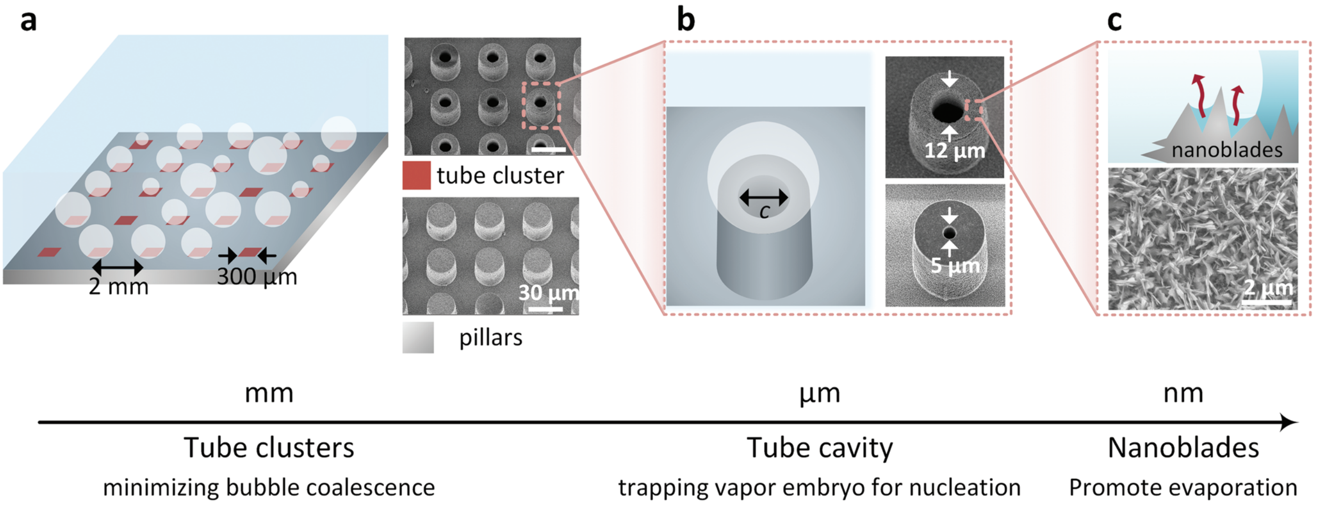

Figure 1. Schematics and scanning electron microscopy (SEM) images of a hierarchically structured TIP surface (h-TIP) that exhibits capillary wicking while controlling vapor nucleation using multiple length scales. a) The h-TIP surface consists of hierarchical tube clusters interspersed in hierarchical pillar arrays. Left: 2 mm pitch between the tube clusters separates bubbles and minimizes bubble coalescence. The dark-red patterned regions represent the hierarchical tube clusters whereas the gray region is covered by hierarchical pillar structures. Right: SEM images of the hierarchical tube structures (top) and hierarchical pillar structures (bottom). Scale bars: 30 µm. b) Microscale cavity at the center of tube structure traps vapor embryo and promotes nucleation. Left: schematic of bubble nucleation on the top of a tube structure. Right: SEM images of a hierarchical tube with a cavity diameter of 12 µm (top) and 5 µm (bottom). c) Nanoblades on top of microstructures augment liquid evaporation under the bubbles. Top: schematic of the extended liquid–vapor interface on the nanostructures. Bottom: SEM image of the nanostructures created all over the h-TIP and h-Tube surfaces including their tubes, pillars, and flat base.

In addition, certain copper-based engineered surfaces have shown simultaneous enhancements of HTC and CHF,[11] but the change in surface morphology and chemical composition of copper surfaces by in situ oxidation during boiling has made the enhancement mechanism unclear.[12]

In this work, we overcome this trade-off and demonstrate an approach to achieve simultaneous extreme enhancement of HTC and CHF based on chemically stable SiO_2 surfaces. By designing a three-tier hierarchically structured TIP surface (h-TIP), we can control vapor nucleation at multiple length scales while providing capillary wicking (**Figure 1**). For CHF enhancement, we minimized bubble coalescence and exploited capillary wicking by defining separated nucleation sites with tube clusters (shaded dark-red area in Figure 1a). For HTC enhancement, on the other hand, we promoted vapor nucleation with microscale cavities (Figure 1b), where evaporation could be further enhanced by extending the liquid–vapor interfaces on nanostructures (Figure 1c). Our strategy to enhance HTC does not have the detrimental effect of continuing to increase the nucleation-site density and as a result, prevents the liquid rewetting process.

2. Results and Discussion

We fabricated hierarchically structured TIP surfaces (h-TIP) along with uniform arrays of hierarchically structured tubes (h-Tube), which consist of only tubes, to investigate the effectiveness of bubble separation by TIP structures in the presence of nanostructures. First, microscale structures were created through photolithography and deep reactive ion etching processes on silicon wafers. The outer diameter, height, and pitch of microtubes and micropillars were fixed at 22, 30, and 40 µm, respectively. To investigate the effects of cavity size on the onset of nucleate boiling temperature, two cavity diameters of 5 and 12 µm were fabricated (SEM images in Figure 1b) for both h-Tube and h-TIP surfaces. According to the theoretical analysis for active cavity sizes for nucleate boiling,[13] 5 and 12 µm cavities were chosen to initiate vapor nucleation at 11 and 5 °C wall superheats, respectively.[10] The cluster-to-cluster pitch was set to 2 mm based on the capillary length of water (≈2.5 mm) (Figure 1a), which has been found as an optimal distance between nucleation sites for effective separation of vapor bubbles in previous works.[10,14] On top of the microstructured surfaces, sharp blade-like cupric oxide (CuO) nanostructures were created by sputtering a 500 nm copper layer over the microstructures followed by oxidation in an alkali solution ($NaClO_2$, NaOH, Na_3PO_4, and deionized water with 3.75:5:10:100 wt%) at 95 °C for 2 min (SEM image in Figure 1c).[15] The structural durability of CuO nanostructures during boiling has been demonstrated in previous studies.[16] In the end, we deposited a 20 nm silicon dioxide (SiO_2) layer using atomic layer deposition to ensure uniform hydrophilicity along the entire hierarchical structure.

The pool boiling experiments were performed with saturated high-purity deionized water at atmospheric conditions by applying heat flux through a serpentine platinum (Pt) heater on the backside of each sample. This Pt heater was also used for thermometry based on its linear correlation between electrical resistance and temperature. Prior to boiling, all surfaces were cleaned with solvents followed by an argon plasma to remove organic contaminants.[17] The bubble dynamics during boiling were captured by a high-speed camera (Phantom v7.1, Vision Research) with up to 4000 frames per second.

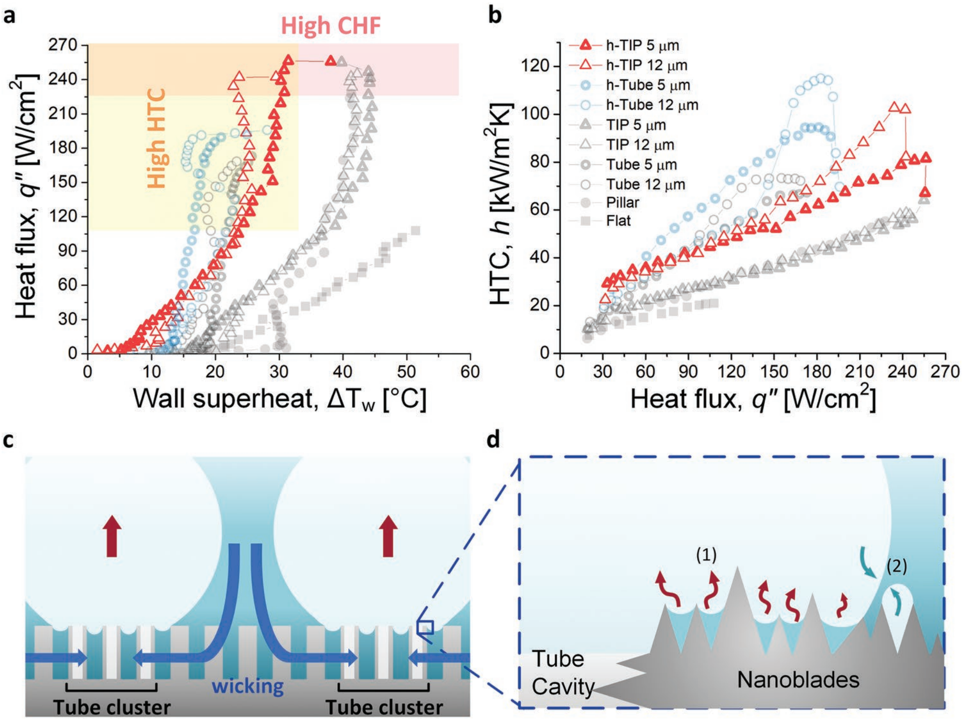

Figure 2. Pool boiling results and schematics of boiling heat transfer enhancement on h-TIP surfaces. a) Pool boiling curves of saturated water on h-Tube and h-TIP surfaces compared with microstructured surfaces without nanostructures. b) HTC as a function of heat flux. The experimental uncertainty is smaller than the marker size. c) Schematic of the separated liquid–vapor paths during boiling on an h-TIP surface. Bubbles grow on top of and depart from tube clusters, while liquid coming outside tube clusters rewets the surface by capillary wicking. d) Schematic explanation of the two mechanisms for the nanostructure-induced evaporation: 1) rapid evaporation of thin liquid films due to their nanoscale thickness and 2) diffusion of vapor trapped in nanostructures, which accelerates bubble growth and departure.

Figure 2a shows pool boiling curves, that is, heat flux as a function of wall superheat, of h-TIP and h-Tube surfaces along with microstructured surfaces with the same microscale dimensions such as micropillars, microtubes, and TIP surfaces from the previous work for comparison.[10] Each surface is named with its structure and the cavity diameter; for example, h-TIP 12 μm is an h-TIP surface that has a 12 μm diameter cavity in each tube cluster. We also plotted HTC as a function of heat flux in Figure 2b. All hierarchical structures showed enhanced HTC and CHF values compared with their microstructure counterparts without nanostructures. For example, h-TIP surfaces significantly enhanced HTC values while maintaining the high CHF of TIP surfaces. Compared with up to 209% enhancement (relative to a flat surface) of maximum HTC ($h_{\max}$) on normal TIP surfaces, h-TIP 5 μm and h-TIP 12 μm achieved 289% and 389% enhancement, respectively. At the same time, the CHF values of h-TIP 5 μm and h-TIP 12 μm were enhanced by 138% and 125%, respectively. In fact, the boiling curves of h-TIP surfaces shifted left of the boiling curves of normal TIP surfaces. This simultaneous enhancement of HTC and CHF on h-TIP structures was achieved because the nanostructures extended the liquid–vapor interface. As a result, this effect promoted evaporation and enhanced HTC. Meanwhile, the nucleation-site density was maintained (Figure 2c,d) to prevent hindering the liquid rewetting, which would limit CHF enhancement. We attribute two mechanisms within the nanostructures for promoting evaporation and bubble departure frequency. First, the liquid imbibed in the nanostructures can evaporate quickly under the vapor bubbles because of the nanoscale liquid film thickness (mechanism (1) in Figure 2d). Second, when the nanostructures are filled with vapor, the vapor can diffuse and merge with a growing bubble above them, which will accelerate the bubble growth and departure frequency (mechanism (2) in Figure 2d).

A similar enhancement was observed on h-Tube surfaces compared with normal microtube surfaces due to the enhanced evaporation from the nanostructures. The maximum HTC value of h-Tube 5 μm and h-Tube 12 μm, for example, were 351% and 448% enhancement, respectively. This result is a significant improvement compared with the 244% enhancements of $h_{\max}$ on normal microtube arrays. In addition to the HTC enhancement, h-Tube surfaces demonstrated higher CHF enhancement than microtube surfaces, where h-Tube 5 μm and h-Tube 12 μm achieved 78% and 82% CHF enhancement, respectively, while Tube 12 μm showed 62% CHF enhancement. Because the extensively high nucleation-site density primarily triggered the boiling crises on h-Tube and microtube surfaces, the addition of nanostructures was able to enhance CHF as well as HTC by providing additional evaporation heat flux for a similar nucleation-site density near CHF. Yet, the CHF enhancement was still limited compared to TIP and h-TIP surfaces. The pool boiling results of h-TIP and h-Tube surfaces confirm that our h-TIP surfaces maintained the high CHF values of TIP surfaces while significantly improving the HTC because of the effective separation of liquid and vapor paths during boiling, which also allows surfaces to exploit the capillary wicking completely (Figure 2c).

Another interesting observation to note was that hierarchical surfaces with 12 µm cavity diameters (h-Tube 12 µm and h-TIP 12 µm) showed a decrease in wall superheat near 20 °C while the heat flux increased, a phenomenon known as boiling inversion. However, a similar phenomenon was not observed on hierarchical surfaces with 5 µm cavity diameters. While previous works attributed the boiling inversion primarily to enhanced macro-convection driven by effective separation of liquid–vapor paths,[18] another work showed that the boiling inversion disappeared when boiling curves were obtained by decreasing heat flux,[19] which cannot be explained by the macro-convection hypothesis. Interestingly, our h-TIP 12 µm surface showed boiling inversion even on the boiling curve obtained by decreasing heat flux. Understanding of the boiling inversion mechanism is still limited and needs further investigation. A detailed discussion on experimental repeatability and boiling inversion is available in Section II of the Supporting Information.

We confirmed the different behavior of bubble interactions on h-Tube and h-TIP surfaces by capturing the bubble dynamics with a high-speed camera up to 4000 frames per second. High-speed movies are available in the Supporting Information. **Figure 3** shows images capturing the bubble dynamics on h-Tube and h-TIP surfaces at a moderate heat flux of ≈40 W cm^{-2} (the first row of Figure 3) and at CHF (the second row of Figure 3). Since microscale cavities promote nucleation, significantly higher nucleation-site densities were observed on h-Tube surfaces compared to h-TIP surfaces. Accordingly, bubbles on h-Tube surfaces showed intensive interactions with each other. In the case of h-TIP surfaces, on the contrary, bubbles nucleated from spatially separated tube clusters, which led to a reduced bubble coalescence. This behavior continued until CHF was reached. We observed that vapor films formed over h-Tube surfaces at CHF, which suggests that CHF enhancement was limited because of the high nucleation-site density. The separation of nucleating bubbles on h-TIP surfaces, on the other hand, was effective even at CHF; therefore, the CHF on h-TIP surfaces was enhanced until it was limited by capillary wicking. This observation supports our boiling curve analysis that h-TIP surfaces enhanced HTC without increasing the nucleation-site density, resulting in simultaneous enhancement of HTC and CHF.

In **Figure 4**, we compared CHF (q''_{CHF}) and the maximum HTC ($h_{\max}$) values of h-TIP and h-Tube surfaces with different micro/nanostructures from the literature. The structures from the literature include microtube and TIP,[10] micropillar,[7a,20] hierarchically structured pillar (h-Pillar),[21] nanowire,[7d,22] microcavity,[10,23] microridge,[24] and microchannel.[23,25] All data shown in Figure 4 are summarized in Table S1, Supporting Information. Here we compared the data of SiO_2 surfaces, except nanowires based on silicon, to compare the effects of structures excluding the effects of material properties. Our h-TIP surfaces showed the highest simultaneous enhancement of HTC and CHF among all other structures, as shown in the top-right corner of the plot. Yet, there are opportunities for further enhancement of h-TIP surfaces by optimizing microscale structure dimensions such as the outer diameter, pitch, and height of hierarchical tubes and pillars, which were fixed in this work.

q'' ~ 40 W/cm^2

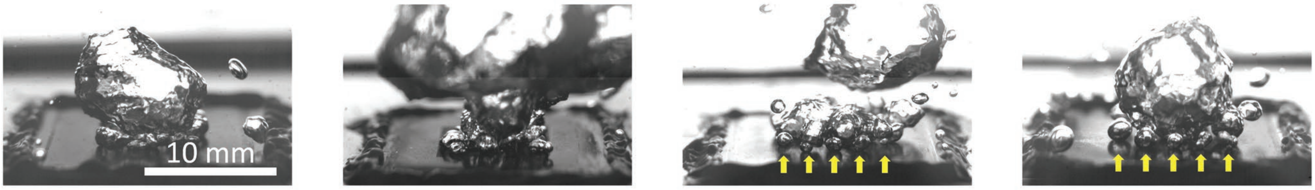

h-Tube 5 µm ΔT_w = 14.1°C q'' = 41.4 W/cm^2

h-Tube 12 µm ΔT_w = 16.2°C q'' = 40.4 W/cm^2

h-TIP 5 µm ΔT_w = 13.0°C q'' = 42.2 W/cm^2

h-TIP 12 µm ΔT_w = 14.2°C q'' = 41.3 W/cm^2

q'' at CHF

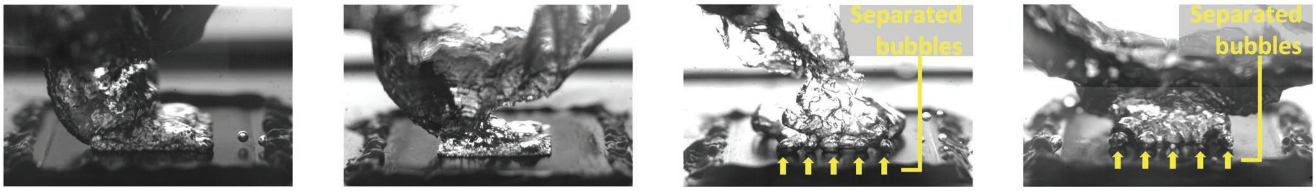

h-Tube 5 µm ΔT_w = 25.0°C q''_{CHF} = 192.1 W/cm^2

h-Tube 12 µm ΔT_w = 28.1°C q''_{CHF} = 195.9 W/cm^2

h-TIP 5 µm ΔT_w = 38.1°C q''_{CHF} = 255.8 W/cm^2

h-TIP 12 µm ΔT_w = 29.5°C q''_{CHF} = 242.3 W/cm^2

Figure 3. Images of bubbles on h-Tube and h-TIP surfaces during boiling were captured by a high-speed camera with a 19° tilt angle and up to 4000 frames per second. The first and second rows show bubble dynamics at a heat flux of ≈40 W cm^{-2} and at CHF, respectively. h-TIP surfaces showed effectively separated bubbles even at CHF (highlighted with yellow arrows), while h-Tube surfaces showed extensive bubble coalescence which led to the formation of vapor films at CHF. High-speed movies are available in the Supporting Information.

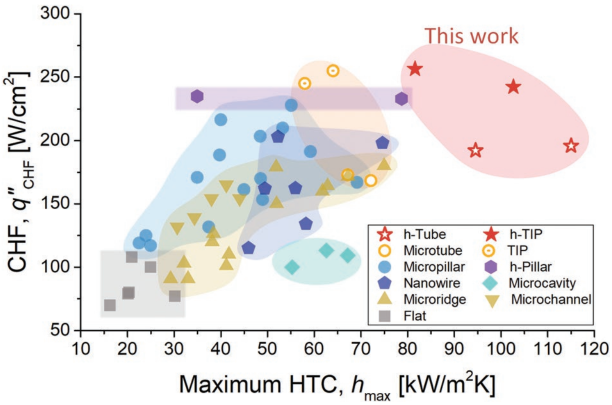

Figure 4. Regime map of CHF (q''_{CHF}) and maximum HTC (h_{max}) values of different SiO_2 micro/nano structures and Si nanowires. This work with h-TIP shows the highest performance (upper right region) with simultaneous CHF and HTC enhancement.

3. Conclusions

We have developed boiling surface structures that achieved superior pool boiling performance via multiscale control of vapor nucleation on hemi-wicking surfaces. Our strategy included the minimization of bubble coalescence, promoting vapor nucleation, and enhancing evaporation by engineering surfaces with separated tube clusters, microscale cavities, and nanostructures, respectively. Meanwhile, capillary wicking performance was maintained in the presence of dynamically interacting boiling bubbles. We conducted saturated pool boiling experiments with water under atmospheric conditions and analyzed the results, with supporting data from high-speed imaging of bubble dynamics. Our hierarchical TIP surfaces (h-TIP) achieved significant HTC enhancement up to 389% as well as 138% CHF enhancement compared to a smooth surface. This work provides surface design guidelines for extreme pool boiling heat transfer, that is, the effective separation of nucleating bubbles, enhanced evaporation by nanostructures, and exploiting capillary wicking are essential. We expect that our design guidelines can be adopted for industry-scale boiling applications by creating surfaces using scalable processes such as sandblasting;[26] for example, a similar hierarchical structure can be created by sandblasting a surface using first a larger abrasive and subsequently a smaller abrasive. Furthermore, physical insights obtained in this work can be utilized in other applications such as electrochemical oxygen or hydrogen evolution reactions, where surface–bubble interactions play a crucial role in their performance.[27] The enhanced boiling performance promises significant energy savings in various boiling applications, including steam power plants, desalination, thermal management of concentrated photovoltaics, etc.

4. Experimental Section

Surface Fabrication: The microscale structures were first fabricated through photolithography and deep-reactive etching processes on silicon wafers that had 1 µm thermal oxide on both sides. A 2 µm layer of photoresist (SPR 700, Microposit) was spin-coated with 3600 rpm for 30 s on one side of the wafers. After pre-baking in a box furnace at 95 °C for 45 min, the photoresist was exposed using an MLA150 Maskless Aligner. The resist was then developed in the developer (CD26, Microposit) followed by post-baking at 120 °C for 30 min. The exposed silicon dioxide layer was etched by reactive ion etching (RIE) (Precision 5000, Applied Materials) with CF_4 as a primary gas. Then, micropillars and microtubes were etched in the bulk silicon with deep reactive ion etching (MESC Multiplex ICP, STS) based on SF_6 and C_4F_8. The processed wafers were treated with oxygen plasma in the RIE chamber to remove the C_4F_8 passivation layers and organic contaminants. To create nanostructures over the microfabricated surfaces, a 500 nm copper (Cu) layer with a 50 nm titanium (Ti) adhesion layer was sputtered. The Cu layer was then oxidized in an alkali solution ($NaClO_2$, NaOH, Na_3PO_4, and deionized water with 3.75:5:10:100 wt%) at 95 °C for 2 min, resulting in sharp blade-like cupric oxide (CuO) nanostructures. Finally, the entire surfaces of hierarchical structures were covered by a 20 nm silicon dioxide (SiO_2) layer using atomic layer deposition.

Pool Boiling Characterization: The pool boiling setup consisted of a glass chamber with an Ultem fixture at the bottom and a PEEK fixture at the top. The test sample (20×20 mm^2) was attached to an Ultem fixture with adhesive sealant (High-temperature RTV Silicone, Permatex). The test sample was fabricated based on a 650 µm-thick silicon substrate. A rope heater was used to maintain the saturation temperature in the glass chamber by preventing heat loss. At the top PEEK fixture, an immersion heater and a reflux condenser were installed. The deionized water was first pre-heated in a separate electric kettle before introducing the water into the glass chamber. The immersion heater was used to degas the pre-heated water by boiling for another 30 min before experimental measurements. During this degassing period, a heat flux of ≈50 W/cm^{-2} was applied. The reflux condenser condensed water vapor and allowed it to return back to the pool as liquid. A power supply (KLP 600-4-1200, Kepco) provided power for the Joule heater of the 10×10 mm^2 heating area (A_h) defined by the serpentine Pt heater on the back side of the sample through Au/Pt electrodes. A multimeter (2110 5½, Keithley) formed a serial connection with the power supply and the sample for the current measurement across the heater (I), while the other multimeter (34401A, Agilent) was connected in parallel for the voltage-drop measurement (V). The input heat flux was then evaluated as $q''_{in} = (I \times V)/A_h$. The Pt backside heater also served as a resistance temperature detector (RTD) for temperature characterization. Prior to pool boiling experiments, test samples were placed in a furnace with a high accuracy Pt RTD (Omega Engineering, RTD-810) close to it. The heater resistance was then measured at six different temperature set points. The dwell time at each set point was at least 2 h to ensure thermal equilibrium within the furnace. The resistance was measured with the four-wire method using a temperature input module (NI-9226 and cDAQ-9171, National Instruments). The experimental data were fit with a linear model. The linear fit was used to convert the measured resistance to the temperature of the heater during pool boiling experiments. Because of the size mismatch between the actual heating area and the exposed surface area, there could be heat loss through the sample thickness. The boiling heat flux and wall superheat based on the measured input heat flux and the heater temperature were numerically calibrated (COMSOL Multiphysics 5.3a LiveLink for MATLAB). In the numerical simulation, the calculations were iterated by changing the heat transfer coefficients at the boiling surface until the calculation of the backside heater temperature matched the experimentally measured temperature. All data points in the boiling curves were calibrated in this manner. Details of the boiling test rig with schematics, experimental procedure, and measurement uncertainty are available in Section I of the Supporting Information.

Supporting Information

Supporting Information is available from the Wiley Online Library or from the author.

Acknowledgements

Y.S. and H.C. acknowledge that the information, data, or work presented herein was funded in part by the Advanced Research Projects Agency-Energy (ARPA-E), U. S. Department of Energy, under Award Number DE-AR0000ABC. C.D.D.-M. acknowledges the Air Force Office of Scientific Research under Grant No. FA9550-19-1-0392 with Dr. Ali Sayir as program manager, and Professor Amar G. Bose Research Grant. L.Z. acknowledges the Singapore-MIT Alliance for Research and Technology (SMART) program. This work was carried out in part through the use of MIT.nano's facilities.

Conflict of Interest

The authors declare no conflict of interest.

Data Availability Statement

The data that support the findings of this study are available from the corresponding author upon reasonable request.

Keywords

critical heat flux, heat-transfer coefficient, hierarchical structures, microstructures, nanostructures, phase-change heat transfer

Received: January 27, 2022
Revised: June 12, 2022
Published online: July 12, 2022

---

[1] bp Statistical Review of World Energy 2020, BP plc, London, UK **2020**.

[2] W. H. Wiser, *Energy Resources: Occurrence, Production, Conversion, Use*, Springer, New York **1999**.

[3] a) T. Mattila-Sandholm, G. Wirtanen, *Food Rev. Int.* **1992**, *8*, 573; b) A. Haryanto, S. Fernando, N. Murali, S. Adhikari, *Energy Fuels* **2005**, *19*, 2098; c) T. Humplik, J. Lee, S. C. O'Hern, B. A. Fellman, M. A. Baig, S. F. Hassan, M. A. Atieh, F. Rahman, T. Laoui, R. Karnik, E. N. Wang, *Nanotechnology* **2011**, *22*, 292001; d) J. D. Hansen, J. A. Johnson, D. A. Winter, *Int. J. Pest Manage.* **2011**, *57*, 267; e) J. Yang, X. Zhang, H. Qu, Z. G. Yu, Y. Zhang, T. J. Eey, Y.-W. Zhang, S. C. Tan, *Adv. Mater.* **2020**, *32*, 2002936; f) D. K. Nandakumar, Y. Zhang, S. K. Ravi, N. Guo, C. Zhang, S. C. Tan, *Adv. Mater.* **2019**, *31*, 1806730.

[4] a) A. Royne, C. J. Dey, D. R. Mills, *Sol. Energy Mater. Sol. Cells* **2005**, *86*, 451; b) Y. Liu, Y. Zhu, Y. Cui, *Nat. Energy* **2019**, *4*, 540; c) K. Ebrahimi, G. F. Jones, A. S. Fleischer, *Renewable Sustainable Energy Rev.* **2014**, *31*, 622; d) L. L. Vasiliev, *Appl. Therm. Eng.* **2005**, *25*, 1.

[5] a) N. E. Todreas, M. S. Kazimi, *Nuclear Systems Volume I: Thermal Hydraulic Fundamentals*, 3rd ed., CRC Press, Boca Raton, FL, USA **2021**; b) J. Buongiorno, *Ann. Nucl. Energy* **2014**, *63*, 9.

[6] a) L. Cheng, D. Mewes, A. Luke, *Int. J. Heat Mass Transfer* **2007**, *50*, 2744; b) H. J. Cho, D. J. Preston, Y. Zhu, E. N. Wang, *Nat. Rev. Mater.* **2016**, *2*, 16092.

[7] a) K.-H. Chu, R. Enright, E. N. Wang, *Appl. Phys. Lett.* **2012**, *100*, 241603; b) M. M. Rahman, E. Ölçeroğlu, M. McCarthy, *Langmuir* **2014**, *30*, 11225; c) N. S. Dhillon, J. Buongiorno, K. K. Varanasi, *Nat. Commun.* **2015**, *6*, 8247; d) R. Chen, M.-C. Lu, V. Srinivasan, Z. Wang, H. H. Cho, A. Majumdar, *Nano Lett.* **2009**, *9*, 548; e) H. Zhao, S. Dash, N. S. Dhillon, S. Kim, B. Lettiere, K. K. Varanasi, A. J. Hart, *ACS Appl. Nano Mater.* **2019**, *2*, 5538.

[8] Y. Song, L. Zhang, C. D. Díaz-Marín, S. S. Cruz, E. N. Wang, *Int. J. Heat Mass Transfer* **2022**, *183*, 122189.

[9] a) Y. Liu, J. Tang, L. Li, Y. N. Shek, D. Xu, *Int. J. Heat Mass Transfer* **2019**, *132*, 25; b) C. K. Yu, D. C. Lu, T. C. Cheng, *J. Micromech. Microeng.* **2006**, *16*, 2092.

[10] Y. Song, S. Gong, G. Vaartstra, E. N. Wang, *ACS Appl. Mater. Interfaces* **2021**, *13*, 12629.

[11] a) C. M. Patil, S. G. Kandlikar, *Int. J. Heat Mass Transfer* **2014**, *79*, 816; b) A. Jaikumar, S. G. Kandlikar, *Int. J. Heat Mass Transfer* **2016**, *95*, 795; c) A. Jaikumar, S. G. Kandlikar, *Appl. Phys. Lett.* **2016**, *108*, 041604; d) S. Zhang, X. Jiang, Y. Li, G. Chen, Y. Sun, Y. Tang, C. Pan, *Energy Convers. Manage.* **2020**, *209*, 112665; e) J. Li, G. Zhu, D. Kang, W. Fu, Y. Zhao, N. Miljkovic, *Adv. Funct. Mater.* **2021**, *31*, 2006249; f) J. Li, W. Fu, B. Zhang, G. Zhu, N. Miljkovic, *ACS Nano* **2019**, *13*, 14080.

[12] Y. Song, H. Cha, Z. Liu, J. H. Seong, L. Zhang, D. J. Preston, E. N. Wang, *Int. J. Heat Mass Transfer* **2022**, *185*, 122320.

[13] a) Y. Y. Hsu, *J. Heat Transfer* **1962**, *84*, 207; b) P. Griffith, J. D. Wallis, *Chem. Eng. Prog., Symp. Ser.* **1958**, *56*, 49.

[14] M. M. Rahman, J. Pollack, M. McCarthy, *Sci. Rep.* **2015**, *5*, 13145.

[15] Y. Nam, S. Sharratt, C. Byon, S. J. Kim, Y. S. Ju, *J. Microelectromech. Syst.* **2010**, *19*, 375.

[16] a) Y. Im, C. Dietz, S. S. Lee, Y. Joshi, *Nanoscale Microscale Thermophys. Eng.* **2012**, *16*, 145; b) K.-H. Chu, Y. S. Joung, R. Enright, C. R. Buie, E. N. Wang, *Appl. Phys. Lett.* **2013**, *102*, 151602; c) M. M. Rahman, M. McCarthy, *J. Heat Transfer* **2017**, *139*, 111508.

[17] Y. Song, L. Zhang, Z. Liu, D. J. Preston, E. N. Wang, *Appl. Phys. Lett.* **2020**, *116*, 253702.

[18] A. Jaikumar, S. G. Kandlikar, *Appl. Phys. Lett.* **2017**, *110*, 094107.

[19] a) J. Costa-Greger, A. Tsubaki, J. Gerdes, M. Anderson, C. Zuhlke, D. Alexander, J. Shield, G. Gogos, in *2020 19th IEEE Intersociety Conf. on Thermal and Thermomechanical Phenomena in Electronic Systems (ITherm)*, IEEE, Piscataway, NJ, USA **2020**, pp. 298–305; b) C. Kruse, A. Tsubaki, C. Zuhlke, D. Alexander, M. Anderson, E. Peng, J. Shield, S. Ndao, G. Gogos, *J. Heat Transfer* **2019**, *141*, 051503.

[20] S. H. Kim, G. C. Lee, J. Y. Kang, K. Moriyama, M. H. Kim, H. S. Park, *Int. J. Heat Mass Transfer* **2015**, *91*, 1140.

[21] K.-H. Chu, Y. Soo Joung, R. Enright, C. R. Buie, E. N. Wang, *Appl. Phys. Lett.* **2013**, *102*, 151602.

[22] a) B. S. Kim, S. Shin, D. Lee, G. Choi, H. Lee, K. M. Kim, H. H. Cho, *Int. J. Heat Mass Transfer* **2014**, *70*, 23; b) M.-C. Lu, R. Chen, V. Srinivasan, V. P. Carey, A. Majumdar, *Int. J. Heat Mass Transfer* **2011**, *54*, 5359; c) Z. Yao, Y. W. Lu, S. G. Kandlikar, *Int. J. Therm. Sci.* **2011**, *50*, 2084.

[23] D. E. Kim, S. C. Park, D. I. Yu, M. H. Kim, H. S. Ahn, *Appl. Phys. Lett.* **2015**, *107*, 023903.

[24] A. Zou, S. C. Maroo, *Appl. Phys. Lett.* **2013**, *103*, 221602.

[25] H. Kim, H. S. Ahn, H. J. Kwak, M. H. Kim, D. E. Kim, *Appl. Phys. Lett.* **2016**, *109*, 243901.

[26] Y. Song, C. Wang, D. J. Preston, G. Su, M. M. Rahman, H. Cha, J. H. Seong, B. Philips, M. Bucci, E. N. Wang, *ACS Appl. Mater. Interfaces* **2022**, *14*, 9788.

[27] a) J. K. Lee, A. Bazylak, *Joule* **2021**, *5*, 19; b) J. K. Lee, C. Lee, K. F. Fahy, B. Zhao, J. M. LaManna, E. Baltic, D. L. Jacobson, D. S. Hussey, A. Bazylak, *Cell Rep. Phys. Sci.* **2020**, *1*, 100147; c) R. Iwata, L. Zhang, K. L. Wilke, S. Gong, M. He, B. M. Gallant, E. N. Wang, *Joule* **2021**, *5*, 887; d) L. Yang, L. Loh, D. K. Nandakumar, W. Lu, M. Gao, X. L. C. Wee, K. Zeng, M. Bosman, S. C. Tan, *Adv. Mater.* **2020**, *32*, 2000971; e) J. R. Lake, Á. M. Soto, K. K. Varanasi, *Langmuir* **2022**, *38*, 3276.